Modelling and Simulation in
Materials Science and Engineering

PAPER • **OPEN ACCESS**

Synergistic coupling of thermomechanical loading and irradiation damage in Zircaloy-4

To cite this article: Daniel J Long *et al* 2024 *Modelling Simul. Mater. Sci. Eng.* **32** 045007

View the article online for updates and enhancements.

You may also like

- *In-situ* TEM observation of the evolution of helium bubbles in Mo during He^+ irradiation and post-irradiation annealing
Yi-Peng Li, , Guang Ran et al.

- Effect of Frenkel pairs on the tensile and shock compression strength of multi-elemental alloys
Sandeep Kumar Singh and Avinash Parashar

- Hardening effect of multi-energy^{W2+}-ion irradiation on tungsten–potassium alloy
Yang-Yi-Peng Song, , Wen-Bin Qiu et al.

This content was downloaded from IP address 3.141.199.243 on 06/05/2024 at 14:44

OPEN ACCESS
IOP Publishing

Modelling and Simulation in Materials Science and Engineering

Modelling Simul. Mater. Sci. Eng. **32** (2024) 045007 (18pp) https://doi.org/10.1088/1361-651X/ad312b

Synergistic coupling of thermomechanical loading and irradiation damage in Zircaloy-4

Daniel J Long[1], **Yang Liu**[1,3,*], **Chris Hardie**[2] **and Fionn P E Dunne**[1]

[1] Department of Materials, Royal School of Mines, Imperial College London, London, United Kingdom
[2] UK Atomic Energy Authority, Culham Science Centre, Oxfordshire, United Kingdom
[3] School of Engineering, University of Leicester, Leicester, United Kingdom

E-mail: yang.liu@imperial.ac.uk

Received 22 November 2023; revised 8 February 2024
Accepted for publication 7 March 2024
Published 3 April 2024

Abstract

This work addresses in-situ synergistic irradiation and thermomechanical loading of nuclear reactor components by linking new mechanistic understanding with crystal plasticity finite element modelling to describe the formation and thermal and mechanical annihilation of dislocation loops. A model of pressurised reactor cladding is constructed to extract realistic boundary conditions for crystal plasticity microstructural sub-modelling. Thermomechanical loads are applied to the sub-model to investigate (i) the unirradiated state, (ii) synergistic coupling of irradiation damage and thermal annihilation of dislocation loops, (iii) synergistic coupling of irradiation damage without thermal annihilation of dislocation loops, and (iv) a post-irradiated state. Results demonstrate that the synergistic coupling of irradiation damage and thermomechanical loads leads to the early onset of plasticity, which is exacerbated by the thermal annihilation of dislocations, while the post-irradiated case remains predominantly elastic

* Author to whom any correspondence should be addressed.

Original content from this work may be used under the terms of the Creative Commons Attribution 4.0 licence. Any further distribution of this work must maintain attribution to the author(s) and the title of the work, journal citation and DOI.

© 2024 Crown copyright

due to substantial irradiation hardening. It is shown that full synergistic coupling leads to localisation of quantities linked with crack nucleation including geometrically necessary dislocations and stress.

Keywords: synergistic, thermomechanical, in-situ irradiation, zirconium alloy, crystal plasticity

1. Introduction

The impact of the synergistic evolution of irradiation damage and thermomechanical loading has not yet been simulated for any material. This paper addresses this systematically using new phenomenological models for temperature and damage-dependant evolution of dislocation loop density in Zircaloy-4, within a crystal plasticity finite element (CPFE) framework. Zircaloy-4 is used to manufacture nuclear reactor fuel cladding and is designed to act as a barrier between radioactive fuel pellets and e.g. water in a pressurised water reactor; it is therefore vital that factors affecting its structural integrity are fully understood. Recently, several studies [1–3] addressed the effect of irradiation on dislocation loop density using transmission electron microscopy (TEM) and advanced x-ray diffraction (XRD) techniques. Topping *et al* [3] demonstrated the thermal instability, and hence recovery of dislocation loops in zirconium alloys across a temperature range relevant to civil nuclear power. Torimaru *et al* [4] showed that after just 15 s of heat treatment at 600 °C–700 °C, the ultimate tensile strength and fatigue life of neutron irradiated (hardened) zirconium cladding tubes were restored to near unirradiated values. Similarly, early Zircaloy-2 data from Howe and Thomas [5] showed increased softening with increasing annealing temperature. Moreover, the flow stress vs. annealing temperature trend from Howe and Thomas [5] closely resembles the dislocation loop density vs. annealing temperature trend presented by Topping *et al* [3], highlighting the important link between irradiation damage, thermal history, and mechanical response. Dislocation loops formed during irradiation lead to both significant hardening and post-yield strain softening behaviour in cladding materials [6], due to the initial pinning and subsequent annihilation of dislocation loops, resulting in channel clearing [7]. The annihilation of an irradiation loop occurs when it interacts with a moving dislocation. Under sufficient stress, the moving dislocation, initially pinned by the loop, can drag and/or annihilate the loop, as described by various authors [8–11]. This results in the formation of so-called dislocation channels, within which plastic deformation is localised. These features are analogous to persistent slip bands (PSBs) which arise during fatigue of metals [12], and have been shown to promote localisation of stress at grain boundaries and fatigue crack nucleation [13, 14]. Hence, a fully coupled model requires fundamental understanding to describe the evolution of dislocation loop density with respect to plastic strain, irradiation dose, and temperature. Recent CPFE modelling advances [15–18], underpinned by in-situ high resolution digital image correlation [19], have offered improved mechanistic understanding of microscale plastic deformation in irradiated materials. However, for investigation of synergistic irradiated loading, experiments reach a practical limit. Ideally, experiments would involve thermomechanical testing with in-situ neutron irradiation. However, the cost, time, and radioactivity issues associated with neutron irradiation render this approach infeasible in most cases. Xu *et al* [20] carried out micro tensile testing of single crystal nickel with in-situ helium ion irradiation, which has less safety implications and is less expensive than neutron irradiation. While this approach is attractive for these reasons, the damage mechanisms associated with helium ion irradiation are fundamentally different and the damage is concentrated at the surface [21], thus the effect of irradiation on bulk properties is unattainable. The major literature gap is in understanding material behaviour under concurrent irradiation damage and thermomechanical loading; while comprehensive, published studies thus far rely on mechanical test data from post-irradiated samples. This work aims to (i) determine if synergistic effects have any major implications in terms of structural integrity compared with conventional post-irradiation testing, (ii) develop understanding of how irradiation-linked damage mechanisms (e.g. channel clearing) are affected at elevated temperatures, and (iii) assess the influence of irradiation damage rate on microstructural damage evolution. Hence, the current paper provides an essential path towards total process-structure-property characterisation of safety-critical components for civil nuclear power (both for fission components, e.g. cladding and reactor pressure vessels, and fusion in-vessel components). Theoretical insights are provided for several industrially relevant case studies.

2. Methodology

CPFE modelling is used to predict microscale deformation in Zircaloy-4 under thermomechanical loads and various irradiation conditions. Electron backscatter diffraction provides the orientation data necessary to link crystallographic properties (elastic and plastic anisotropy, including dislocation slip strengths) with simulated (experimentally measured) microstructures. The various hexagonal close packed (HCP) slip systems in zirconium alloys are shown in figure 1.

The rate of plastic shear on the *i*th slip system is calculated using the mechanistic slip rule in equation (1),

$$\dot{\gamma}^i = \rho_{\mathrm{m}} v_{\mathrm{d}} {b^i}^2 \exp\left(\frac{-\Delta F}{k_{\mathrm{B}} T}\right) \sinh\left(\frac{\langle \tau^i - \tau_{\mathrm{c}}^i \rangle \Delta V}{k_{\mathrm{B}} T}\right) \tag{1}$$

where ρ_{m} is density of mobile dislocations, v_{d} the frequency of attempts for dislocations to overcome thermal energy barriers, b^i the slip system Burgers vector magnitude, ΔF the activation energy, k_{B} the Boltzmann constant, T the temperature, ΔV the activation volume, and τ^i and τ_{c}^i are the absolute applied and critical resolved shear stress (CRSS) for slip system i, respectively. Macaulay brackets are applied to the stress terms which indicate that the slip rate is zero when the applied shear stress is lower than the critical value. Full details of the CPFE framework, including the relevant material constants were previously reported [18].

To capture both hardening and softening effects due to irradiation damage in Zircaloy-4, Hardie *et al* [18] developed a mechanistic CPFE-dislocation-based model. Central to this is the incorporation of an irradiation hardening term (a function of dislocation loop density) within the classical Taylor model. Here, a modified isotropic linear hardening (ISO-LH) model [18] is incorporated, whereby the dislocation loop density is treated as equivalent to other dislocation types. The CRSS is then given by equation (2),

$$\tau_{\mathrm{c}}^i = \tau_0^i + \mu b \sqrt{\rho_{\mathrm{SSD}} + \rho_{\mathrm{GND}} + \rho_{\mathrm{loop}}} \tag{2}$$

where τ_0^i is the intrinsic material CRSS (measured experimentally [22]), μ is shear modulus, ρ_{SSD} is the density of statistically stored dislocations (SSDs), whose evolution is linear with plastic strain [23], ρ_{GND} is the density of geometrically necessary dislocations (GNDs) [24], and ρ_{loop} is the total density of dislocation loops, which form during irradiation. Temperature-dependant elastic-plastic properties [23] are also incorporated. SSD density evolution is controlled by $\rho_{\mathrm{SSD}} = \gamma^{\mathrm{st}} p$, where p is cumulative plastic strain and γ^{st} is a material constant. ρ_{GND}

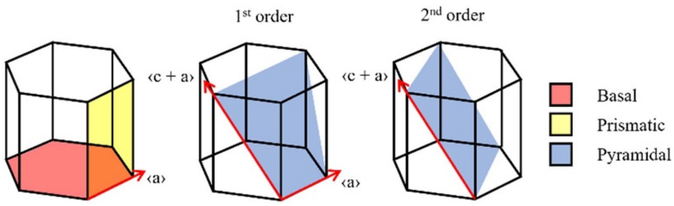

Figure 1. Crystallographic slip systems in HCP unit cell. There are five distinct slip system types: basal ⟨a⟩, prismatic ⟨a⟩, 1st order pyramidal ⟨a⟩, 1st order pyramidal ⟨c + a⟩, and 2nd order pyramidal ⟨c + a⟩.

Table 1. Important material properties. Dislocation loop radius is consistent with the range of experimentally measured values [6, 40, 45]. The critical annihilation temperature and annihilation probability are estimated in the current work.

Parameter	Symbol	Value	Unit
Strain hardening constant	γ^{st}	130	$\mu\mathrm{m}^{-2}$
Annihilation probability (ISO-LH)	ψ^{1-30}	0.005	—
Loop formation probability constant	η	5.30×10^{8}	m^{-1}
Atomic number density	N	4.29×10^{28}	m^{-3}
Mean dislocation loop area	$\bar{A}_{\mathrm{loop}}$	7.1×10^{-6}	$\mu\mathrm{m}^{2}$
Dislocation loop radius	r_{loop}	1.5×10^{-3}	$\mu\mathrm{m}$
Critical annihilation temperature	$T_{0.5}$	648	K

is calculated based on gradients of plastic strain [25], the implementation of which has been described by Xu *et al* [26]. Note that for industrially relevant irradiation doses, the ⟨c⟩ dislocation loop density is negligible [27], since experimental TEM observations have identified that ⟨c⟩ loops only form at doses >10 dpa [28]. Hence, only ⟨a⟩ loops are considered here. In the ISO-LH model, the density of dislocation loops varies equally on each ⟨a⟩ plane as a function of plastic strain, i.e. the softening behaviour is controlled by the annihilation of dislocation loops. The annihilation rate (due to slip) of total ⟨a⟩ loop density is given in differential form in equation (3) [18],

$$\left[\frac{\partial \rho_{\mathrm{loop}}}{\partial t}\right]_{\dot{\gamma}} = -N_{\langle a\rangle} \sum_{i=1}^{N_{\mathrm{sys}}} \psi^{i} \frac{\left|\dot{\gamma}^{i}\right| \sqrt{\frac{\rho_{\mathrm{loop},t}}{N_{\langle a\rangle}}}}{b^{i}} \tag{3}$$

where t is time, $N_{\langle a\rangle} = 3$ is the number of ⟨a⟩ directions, N_{sys} is the total number of HCP slip systems, and ψ^{i} is the annihilation probability for slip system i. Key properties are provided in table 1. As shown in figures 2 (a) and (b), the ISO-LH model is applied to a polycrystalline microstructure to capture room temperature macroscale stress-strain responses in Zircaloy-4 at different irradiation doses (from 0 dpa to 0.8 dpa) [4]. There is strong agreement between model and experiment at each level of irradiation, using a strong basal texture (c-axes predominantly perpendicular to the loading direction) to best represent samples cut from a rolled sheet [6]; the texture was randomly generated with c-axes constrained to remain within 15 degrees of orthogonal to the remote loading direction, i.e. *soft* texture. Initial values for ρ_{loop} were selected for each dose to capture the tensile behaviour. Figure 2 (b) shows the plastic strain distribution after post-irradiation (0.8 dpa) room temperature loading of the polycrystal model.

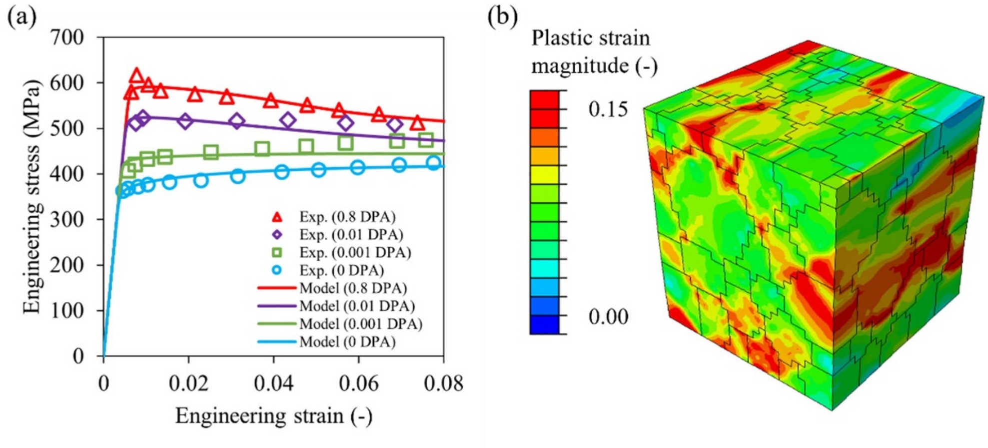

Figure 2. (a) Capturing the polycrystalline response of Zircaloy-4 at different levels of irradiation using the modified isotropic linear hardening model from Hardie *et al* [18]. Experimental data are from Farrell *et al* [6]. (b) Distribution of cumulative plastic strain across 200 grain polycrystal model (0.8 dpa) at a mean applied strain of 8%. Reprinted from [6], Copyright (2004), with permission from Elsevier. Reproduced from [18]. CC BY 4.0.

Highly localised plasticity in the form of shear bands is shown, which leads to the softening behaviour captured in figure 2 (a).

Under synergistic loading, there is competition between the formation of dislocation loops due to irradiation, their thermal annihilation, and their mechanical annihilation, as governed by equation (3). New phenomenological models are proposed to fully describe the evolution of dislocation loops and to link irradiation dose with loop density. The number of displacements per unit volume is given by multiplying the irradiation dose, φ (with units dpa) by the atomic number density, N (with units m^{-3}) [29]. The mean spacing between defects is therefore given by $l_{\mathrm{d}} = \frac{1}{\sqrt[3]{\varphi N}}$. Since dislocation loops are formed by the coalescence of defects, the mean loop spacing is determined by multiplying the defect spacing by the ratio of defects to dislocation loops. For a planar circular dislocation loop, this is given by the ratio of dislocation loop to atomic defect areas. Hence, mean dislocation loop spacing is $l_{\mathrm{loop}} = l_{\mathrm{d}} \cdot \frac{\bar{A}_{\mathrm{loop}}}{N^{-1}/a}$, where $\bar{A}_{\mathrm{loop}}$ represents the mean planar area of dislocation loops and a is atomic spacing; note that in this simple preliminary model, the mean dislocation loop area is assumed constant, and is consistent with TEM-based dislocation loop diameter measurements in zirconium alloys [6] (see table 1). If all defects contribute to the formation of dislocation loops, the theoretical maximum areal dislocation loop density is simply $\rho_{\mathrm{loop}} = l_{\mathrm{loop}}^{-2}$. However, due to replacement collisions and recombination during the thermal spike of the collision cascade, only a small fraction of these displacements remain within the lattice as primary defects [30–32]. Additionally, many defects are lost over larger timeframes during irradiation due to recombination [33] or migration to sinks [34], the probability of which increases with dose (this is evident from creation-relaxation algorithm (CRA) modelling of irradiation damage which predicts that both vacancy and interstitial concentrations saturate with increasing dose, and that the interstitial concentration can undergo a period of substantial decline with increasing damage [35]). Finally, only a fraction of surviving defects are likely to agglomerate forming dislocation loops. Due to the physical processes described above, the actual dislocation loop density is calculated by

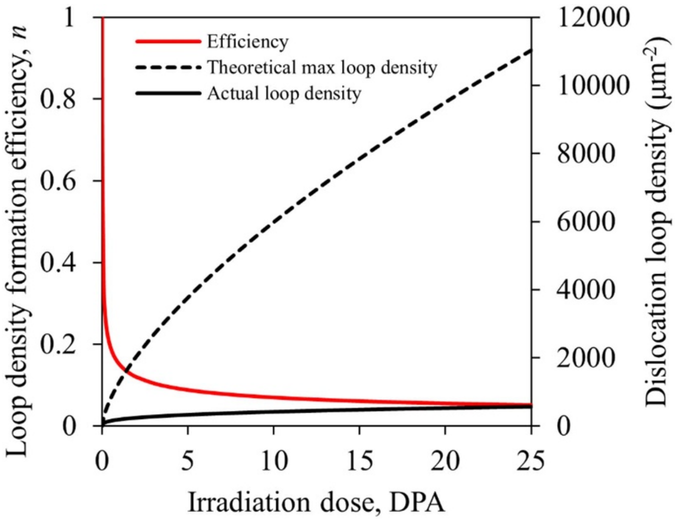

Figure 3. Evolution of loop density efficiency, and corresponding theoretical maximum and actual (fitted model) dislocation loop densities with increasing irradiation dose.

multiplying the theoretical maximum dislocation loop density by an efficiency term, n, which is assumed proportional to defect spacing as follows,

$$n = \eta l_{\mathrm{d}} = \frac{\eta}{\sqrt[3]{\varphi N}} \tag{4}$$

where η is a material-specific empirical constant (with units m^{-1}) used for fitting, i.e. the efficiency of loop formation, n, decreases with increasing irradiation dose. The defects which are lost during irradiation are accounted for by the efficiency factor, giving $\rho_{\mathrm{loop}} = n l_{\mathrm{loop}}^{-2}$ [31, 32]. Hence, dislocation loop density is given by equation (5),

$$\rho_{\mathrm{loop}} = \frac{\eta (\varphi N)^{\frac{1}{3}}}{a^2 \bar{A}_{\mathrm{loop}}^2 N^2}. \tag{5}$$

Using the property values in table 1, an estimate for η is enabled based on TEM measurements of dislocation loop density [2, 3, 6] at various irradiation doses. The influence of the loop density formation efficiency term, n is presented in figure 3 using these properties. It is shown that for irradiation damage levels beyond 3 dpa, the efficiency is below 10%, which is consistent with results from a detailed numerical analysis of damage accumulation by Stoller and Mansur [36]. As shown in figure 4 (a), the overall experimental data trend is captured reasonably well by the model from 0 to 25 dpa, including the aforementioned dislocation densities from the ISO-LH model. It is important to note that equation (5) suggests that as the irradiation damage level approaches infinity, so too will dislocation loop density, while it has been reported to saturate experimentally [1, 37, 38]. The preliminary loop density-damage model is based on interactions with other defects and does not entirely capture the phenomena responsible for saturation at higher doses (e.g. recombination, grain boundary density, and other sinks) and is therefore only applicable within the irradiation dose range for which experimental data are currently available (see figure 4 (a), i.e. $0 < \varphi < 25$ dpa). Moreover, 25 dpa is above conventional reactor cladding irradiation dose limits [39].

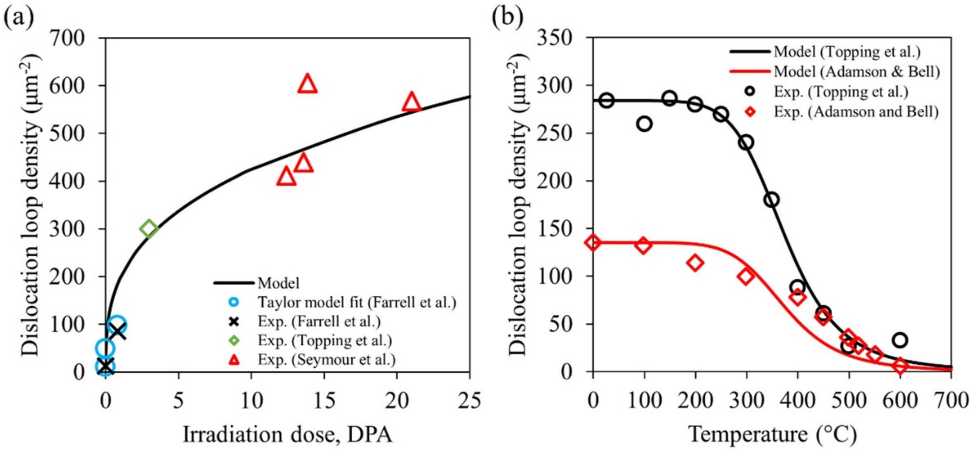

Figure 4. (a) Comparison of the new model for dislocation loop density as a function of irradiation dose with stress-parameterised values, and experimental TEM measurements from Farrell *et al* [6], Topping *et al* [3], and Seymour *et al* [2]. (b) Comparison of model for steady-state annealing of dislocation loops with experimental data from Topping *et al* [3] and Adamson and Bell [46]. Reprinted from [6], Copyright (2004), with permission from Elsevier. Reproduced from [2]. CC BY 4.0. Reprinted from [3], Copyright (2018), with permission from Elsevier.

Recent experiments [3] demonstrated that heat treatment of irradiated zirconium alloys can lead to significant thermal annihilation of dislocation loops. This effect is incorporated into the current framework based on the bulk diffusion mechanism proposed by Eyre and Maher [40]. This mechanism suggests that the growth and shrinkage, and hence annihilation of dislocation loops is controlled by the diffusion of point defects to and from dislocation loops. Further, it is assumed that interstitial diffusion is dominant (despite the high formation energy compared with vacancies [41], interstitials arise due to the formation of Frenkel pairs [42]), as the migration energy of interstitials is much lower than that of vacancies [43], and so the interstitials migrate rapidly to the various sinks, including grain boundaries, interstitial loops, vacancy loops, dislocations, surfaces, etc. For a perfectly circular dislocation loop, the line tension is given by Hirth and Lothe [44] as $\tau_{\mathrm{loop}} = \frac{\mu b^2}{4(1-\nu)}\ln(\frac{4r_{\mathrm{loop}}}{b})$, where ν is Poisson's ratio. The elastic energy released per vacancy emission is given by $w = \frac{\tau_{\mathrm{loop}}V_{\mathrm{at}}}{r_{\mathrm{loop}}b}$ [45] where V_{at} is the characteristic atomic volume ($V_{\mathrm{at}} = N^{-1}$). From statistical mechanics, the concentration of interstitials in equilibrium with a loop is given by $c_{\mathrm{I}} = c_0\exp(-\frac{w}{k_{\mathrm{B}}T}) = c_0\exp(-\frac{\tau_{\mathrm{loop}}V_{\mathrm{at}}}{r_{\mathrm{loop}}bk_{\mathrm{B}}T})$ [45], where c_0 is the thermal equilibrium concentration of interstitials in the bulk. Conversely, for vacancy loops, interstitial emission results in a decrease in elastic energy, and hence, the local vacancy concentration in equilibrium with a loop is $c_{\mathrm{V}} = c_0\exp(\frac{\tau_{\mathrm{loop}}V_{\mathrm{at}}}{r_{\mathrm{loop}}bk_{\mathrm{B}}T})$. For a given irradiation dose, an initial dislocation loop density, $\rho_{\mathrm{loop},0}$ is defined, corresponding to values measured using TEM at room temperature [3]. The temperature-dependant loop density is the difference between the initial value and the density of annihilated dislocations, $\rho_{\mathrm{loop}} = \rho_{\mathrm{loop},0} - \rho_{\mathrm{an}} = \frac{\rho_{\mathrm{loop},0}}{1+\frac{\rho_{\mathrm{an}}}{\rho_{\mathrm{loop}}}}$. Assuming an annihilation event occurs for every vacancy and interstitial interaction, there is a positive linear relationship between their concentrations. Since the diffusion of an interstitial defect can lead to annihilation of both vacancy and interstitial loops, there is also a direct correlation between dislocation density and interstitial concentration. Hence, it is reasonable to assume that the ratio, $\frac{\rho_{\text{an}}}{\rho_{\text{loop}}}$ is proportional to the ratio of interstitial to vacancy concentrations, giving $\frac{\rho_{\text{an}}}{\rho_{\text{loop}}} = \alpha \frac{c_{\text{I}}}{c_{\text{V}}}$, where α is a constant, potentially dependant on composition and microstructure. Applying the temperature dependent equations for vacancy and interstitial concentration gives $\frac{\rho_{\text{an}}}{\rho_{\text{loop}}} = \alpha \exp(-\frac{2\tau_{\text{loop}} V_{\text{at}}}{r_{\text{loop}} b k_{\text{B}} T})$. At temperature $T_{0.5}$, the initial dislocation loop density is reduced by half, $\rho_{\text{loop}} = \frac{\rho_{\text{loop},0}}{2}$, such that $\frac{\rho_{\text{an}}}{\rho_{\text{loop}}} = 1$. This gives $\alpha = \frac{1}{\exp\left(-\frac{2\tau_{\text{loop}} V_{\text{at}}}{r_{\text{loop}} b k_{\text{B}} T_{0.5}}\right)}$. Dislocation loop density is then,

$$\rho_{\text{loop}} = \frac{\rho_{\text{loop},0}}{1 + \exp\left(\frac{2\tau_{\text{loop}} V_{\text{at}}}{r_{\text{loop}} b k_{\text{B}}} \left(\frac{1}{T_{0.5}} - \frac{1}{T}\right)\right)}. \tag{6}$$

As shown in figure 4 (b), this new model captures experimental TEM measurements [3, 46] at different irradiation doses, i.e. two datasets representing different initial dislocation densities at room temperature.

With the dislocation loop density now described as a function of plastic strain, irradiation dose, and temperature, its fully coupled time-dependant evolution is written in differential form as,

$$\frac{d\rho_{\text{loop}}}{dt} = \left[\frac{\partial \rho_{\text{loop}}}{\partial t}\right]_{\dot{\gamma}} + \frac{\partial \rho_{\text{loop}}}{\partial \varphi} \cdot \frac{\partial \varphi}{\partial t} + \frac{\partial \rho_{\text{loop}}}{\partial T} \cdot \frac{\partial T}{\partial t} \tag{7}$$

where $\frac{\partial \rho_{\text{loop}}}{\partial \varphi}$ and $\frac{\partial \rho_{\text{loop}}}{\partial T}$ are given by differentiating equations (5) and (6), respectively, and $\frac{\partial \varphi}{\partial t}$ and $\frac{\partial T}{\partial t}$ are loading conditions. Note that the temperature dependant evolution of loop density is subject to the constraint $\frac{\partial \rho_{\text{loop}}}{\partial T} = 0$ where $\partial T \leqslant 0$, i.e. decreasing the temperature has no direct effect on loop density. Moreover, it is assumed that the timescales considered here (several hours) are sufficient to apply the steady state model in equation (6), i.e. transient effects are negligible.

Industrially relevant stress-controlled boundary conditions are imposed onto a 50×50 µm microstructure section from Thomas *et al* [19], as shown in figure 5 (a). For the mesh, 0.25 µm quadratic brick elements are used. From previous modelling work of a similar microstructure (with channel clearing effects) [18], 0.5–1 µm elements were deemed sufficiently small for mesh convergence. To simulate stress levels sufficient to initiate channel clearing phenomena in irradiated fuel cladding, a global model is constructed with an internal pressure commensurate with high levels of burn-up [47], and is notched at the outer surface (representing a surface defect due to e.g. interfacial cracking with the oxide layer [48], hydride blistering [49], etc). Bulk isotropic elastic-plastic material properties are used in the global model. As shown in figure 5 (a), both normal and shear stress boundary conditions are extracted from the global model and applied to the sub-model. Plane strain boundary conditions are imposed in each case, which are representative of a pipe. Figure 5 (b) shows the thermomechanical loading conditions applied to the sub-model; three repeating thermomechanical cycles [23] are used to study cyclic plasticity. One case of irradiation damage evolution up to 6 dpa is also presented in the figure, which shows the synergistic coupling of damage and thermomechanical loading.

The four cases presented here are summarised as follows,

i. Unirradiated. Thermomechanical loads are applied to unirradiated material and hence, $\rho_{\text{loop}} = \frac{\mathrm{d}\rho_{\text{loop}}}{\mathrm{d}t} = 0$ throughout.

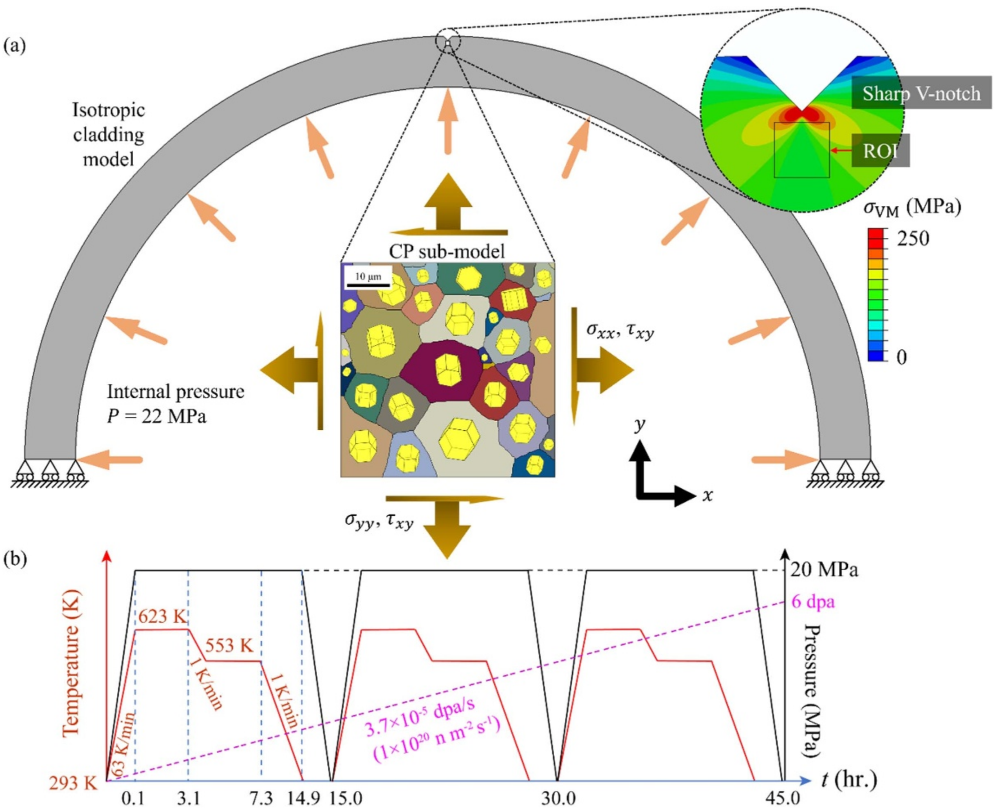

Figure 5. (a) Schematic illustration of notched cladding model and CPFE sub-model. The notched cladding model is used to extract normal and shear stress distributions around the region of interest, for application to the sub-model. The Von Mises stress distribution, in relation to the ROI is shown. Stresses are extracted at the beginning and end of the first cycle and are assumed unchanged for subsequent cycles. Internal and external cladding diameters are 8.8 and 10 mm, respectively. Notch depth is 50 μm. (b) Thermomechanical cycles used for each simulation from Liu *et al* [23]. The selected maximum internal pressure is increased at the beginning of each cycle, held constant, and decreased, while there are two separate dwell periods for temperature. A single example of irradiation dose evolution is shown, whereby the equivalent level of damage increases linearly to 6 dpa over three thermomechanical cycles. This a simplification for the purpose of this preliminary study. For demonstration purposes, a large dose rate is selected to reach 6 dpa within just a few cycles. Reprinted from [23], Copyright (2021), with permission from Elsevier.

ii. Full synergistic coupling. Thermomechanical loads are applied synergistically with linearly increasing irradiation damage, corresponding to a very high constant neutron flux of 1.0×10^{20} n m^{-2} s^{-1} [50], which gives a damage rate, $\frac{\partial \varphi}{\partial t} = 3.7 \times 10^{-5}$ dpa s^{-1}. The equivalent irradiation damage level after three cycles is 6 dpa.
iii. Partial synergistic coupling. Irradiation dose evolution remains coupled with thermomechanical loads, while thermal annihilation of dislocation loops is unaccounted for, i.e. $\frac{\partial \rho_{\text{loop}}}{\partial T} = 0$.
iv. Post-irradiated. The material is pre-irradiated to 6 dpa of damage (consistent with coupled cases) prior to loading. Initial dislocation loop density is estimated using equation (5).

Neutron flux is set to 0, i.e. $\frac{\partial \varphi}{\partial t} = 0$. Unlike previous studies [18], the thermal recovery of dislocation loops at elevated temperatures is accounted for here using equation (7).

An additional set of results with a reduced pre-irradiation damage level (0.6 dpa) is also presented for contrast. For cases of full and partial coupling, this corresponds to a damage rate of 3.7×10^{-6} dpa s^{-1}, which is more comparable to e.g. a realistic pressurised water reactor environment (typically in the range 10^{-7}–10^{-6} dpa s^{-1} for reactor core components [51, 52]); the implications of artificially increasing the irradiation damage rate this for structural integrity are perused in the appendix. Nevertheless, results from high damage rate studies enable qualitative and semi-quantitative assessment of the long-term synergistic effects of irradiation damage and thermomechanical loading, while minimising computational cost.

3. Results and discussion

The results of cases i–iii are presented in figure 6 after three cycles, showing distributions of plastic strain, dislocation loop density, GND density, maximum slip, and stress.

Contour plot results for the post-irradiated case have been omitted from figure 6 as irradiation hardening was predicted to prevent the onset of plastic deformation in the simulation (under the current loading conditions), even after three cycles. Figures 6 (a)–(c) also highlight that irradiation hardening effects under full and partial coupling somewhat inhibit plastic deformation compared with the unirradiated case. Specifically, most plastic deformation under full and partial coupling occurs within the first cycle due to progressive irradiation hardening, while there is a greater cyclic evolution in the unirradiated microstructure. Plastic strain fields from partial coupling demonstrate the importance of accounting for the thermal annihilation of dislocation loops, as the localisation of plasticity is intensified in the fully coupled case, which promotes channel clearing. Channel clearing is particularly evident in the grain highlighted in figure 6 (c); parallel bands containing negligible dislocation loop density (which correlate with bands of high plastic strain) spanning the grain are shown in figure 6 (d). Loop density line profiles from full and partial coupling are presented in figure 6 (h) and show that overall loop densities are higher with partial coupling, while local variations are much larger in the fully coupled case, particularly between the first and second (from left to right) channel clearing bands. Curiously, the maximum loop density magnitudes for full and partial coupling along A–A$'$ are close, despite there being large differences otherwise. This indicates that within the grain of interest, channel clearing is the dominant softening mechanism for both cases. Channel clearing is also shown to have a profound effect on the local GND density in figure 6 (e) as there is significant localisation parallel to the channels, with a clear spatial correlation. Figure 6 (i) shows that for full coupling, GND localisation, which is driven by large strain gradients coincides with the largest loop density undulation. By contrast, GND density is shown to be more evenly distributed in the partially coupled model. Severe grain boundary driven strain localisation in the unirradiated material is shown to derive large GND densities, the magnitudes of which are comparable with peak values in the fully coupled case. Maximum shear strain ($\gamma_{\max} = \sqrt{\frac{1}{2}(\varepsilon_{11} - \varepsilon_{22})^2 + \varepsilon_{12}^2}$) is plotted in figure 6 (f) showing bands of high shear strain localisation. However, figure 6 (j) shows that these bands also exist in the unirradiated material, with approximately twice the magnitude. Even lower strain levels with minimal variation are shown with partial coupling. Lastly, figure 6 (g) shows that there is some correlation between GND density and the *x*-direction stress, particularly along the inclined band. However, it is clear from figure 6 (k) that due to interactions between the *soft* grain (*c*-axis $\perp$ *x*-axis major

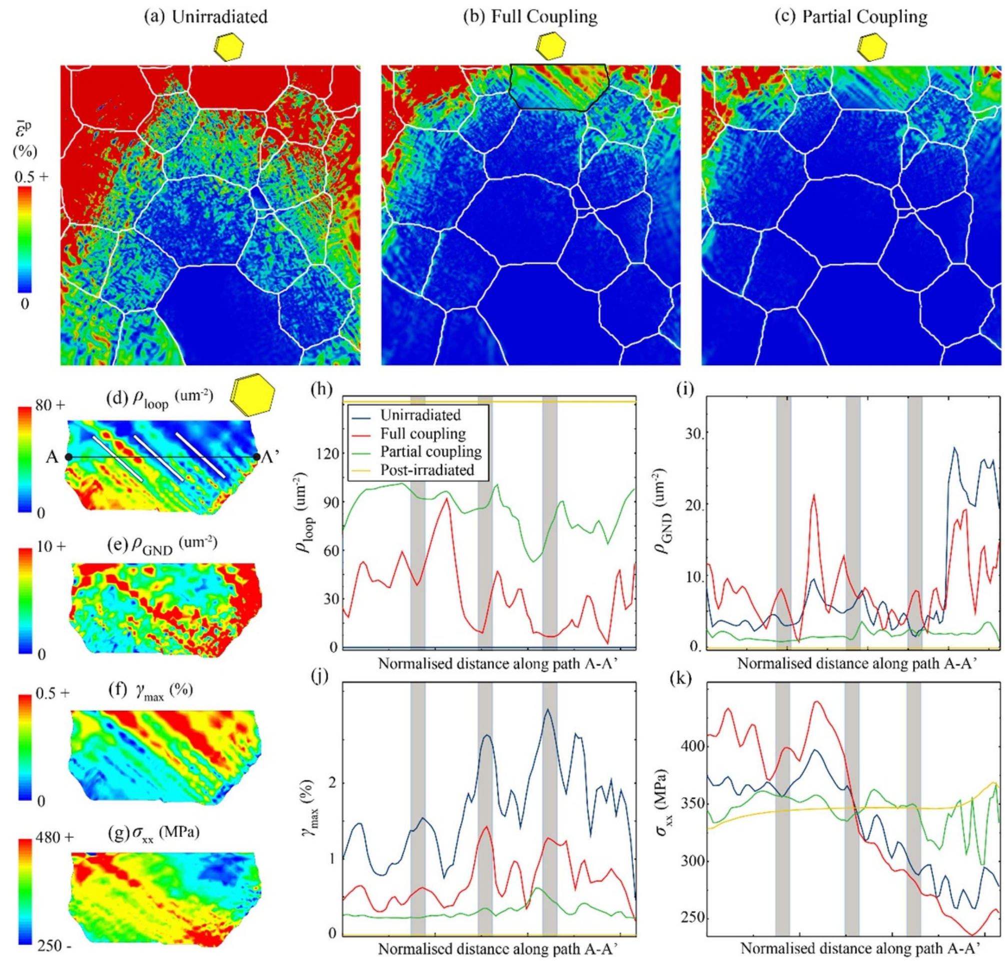

Figure 6. Results of unirradiated, partially coupled, and fully coupled CPFE simulations after three cycles: (a)–(c) plastic strain distributions. For full coupling, within the highlighted grain, (d)–(g) show the dislocation loop density, GND density, maximum shear strain, and x-direction stress distributions, respectively. Line A-A′ is shown in (d), which traverses several ‘channel clearing’ regions, corresponding to drastically reduced dislocation loop density (as indicated by parallel white lines). Line profiles of these variables along line A-A′ are shown for each case in (h)–(k), respectively. Channel clearing regions are indicated by grey shading.

load) of interest and neighbouring *hard* grains (c-axis $\parallel$ x-axis major load), stress shielding is occurring; stresses and strains are re-distributed such that strain localises in the *soft* grain, and stress is localised in *hard* grains. The effect is strongest in the fully coupled case, which also experiences the largest overall stress between the first and second channels, corresponding to the region with maximum GND density. A similar trend is shown in the unirradiated case, but with lower peak stresses and reduced stress re-distribution. Partial coupling shows comparably low stress re-distribution, and roughly follows the elastic, post-irradiated trend. Hence, despite the synergistic coupling of irradiation damage and loading leading to reduced strain localisation (compared with unirradiated material), channel clearing effects are shown to drive significant stress concentrations and localisation of GNDs, both of which have been

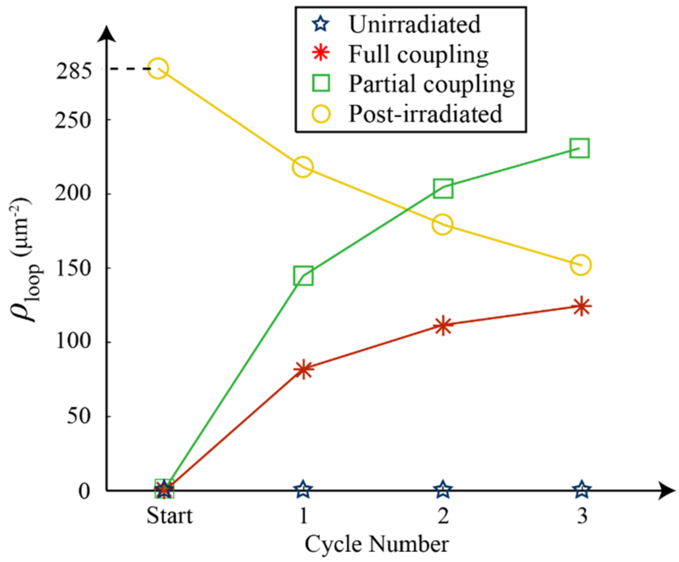

Figure 7. Cyclic evolution of mean dislocation loop density (averaged across entire microstructure) for each case of high irradiation dose investigated.

linked with the nucleation of facets and crack initiation [53]. For future work, it is envisaged that the nucleation of crystallographic fatigue cracks could be compared for each case using, e.g. the stored energy density criterion [53, 54], or a cohesive zones model [55, 56], in which cohesive elements are defined along known slip directions until such a point that the local traction stress exceeds a critical value, leading to fracture.

Figure 7 shows the mean dislocation loop density at the end of each cycle for every high irradiation dose rate case. Full coupling results in a progressive non-linear evolution, which reaches less than half of the initial post-irradiated value (285 μm^{-2}) by the end of the third cycle. Without thermal annihilation, partial coupling shows a more rapid evolution which reaches within 15% of the maximum possible value; this difference is due to plasticity-driven annihilation, while the fully coupled annihilation is due to both thermal and thermally assisted plasticity-driven annihilation. Loop density evolution in the fully elastic post-irradiated material is driven by thermal annihilation only, the rate of which is shown to decrease as loop density magnitude decreases.

Results from the low irradiation dose rate study are presented in figure 8. As with the high dose rate study, the model predicts a progressive non-linear evolution of dislocation loop density with increasing cycle number for full and partial coupling, despite dislocation loop density magnitudes being substantially lower. As shown in the 'Full coupling' grain subfigure, channel clearing is also captured here; however, after just three cycles, the range of dislocation loop density is not significant enough to highlight key distinctions with e.g. the unirradiated case. This demonstrates the utility of high irradiation dose rates from a computational cost perspective since important mechanistic insights are gained without exhausting resources.

Interestingly, the comparably low initial dislocation loop density in the post-irradiated case results in some plasticity-driven dislocation loop annihilation, while virtually none was observed in the high irradiation dose rate due to increased hardening. However, it is clear from the grain subfigures that the resulting loop density distributions are entirely different (to those observed when using full synergistic coupling), and hence, failure mechanisms are likely to

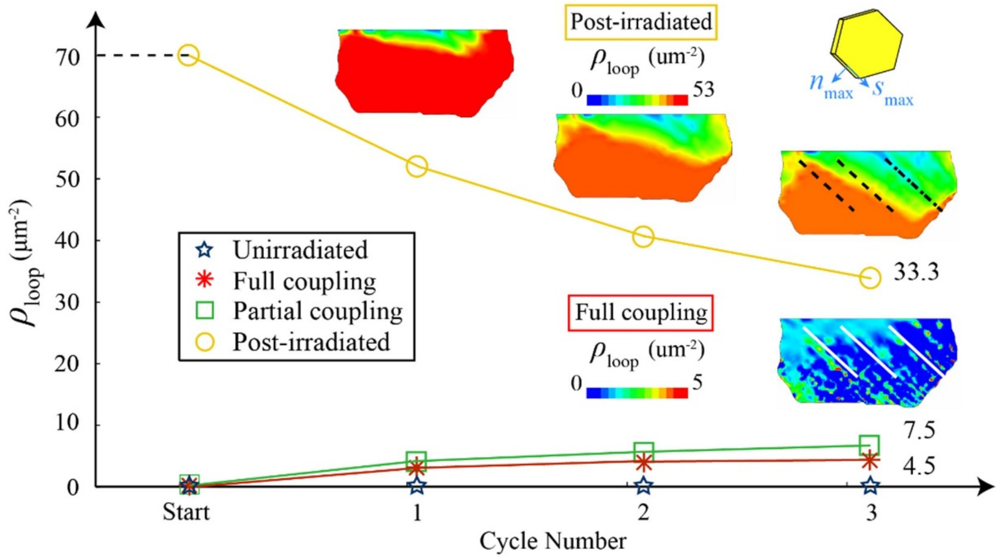

Figure 8. Cyclic evolution of mean dislocation loop density (averaged across entire microstructure) for each case of low irradiation dose investigated, with corresponding dislocation loop density fields in post-irradiated and fully coupled cases.

differ significantly. More specifically, post-irradiated softening is initially dominated by the thermal annihilation of dislocation loops, which gradually leads to plasticity and diffuse loop annihilation (rather than the formation of discrete localised bands). By contrast, the synergistic coupling of irradiation damage is shown to lead to early plastic deformation, the localisation of which is increased due to channel clearing, as compared with no irradiation. This observation underpins the motivation for this paper and brings to the forefront the importance of the synergistic coupling of irradiation damage, temperature, and mechanical load. Hence, there is a need for further research in this area, which will involve greater depth and improved modelling, incorporating e.g. transient effects and loop density saturation using physically based models which are compatible with crystal plasticity, i.e. cluster dynamics [57]. Specifically, models accounting for full temperature-dependant damage evolution and annealing history are required (at present, only temperature dependant loop annihilation is considered). Recent work by Li *et al* [58] showed that cluster dynamics modelling could be coupled with discrete dislocation plasticity to capture the concurrent effects of stress, plasticity, and irradiation damage in zirconium. It is envisaged that upon demonstrating the significance of synergistic effects in this paper, a similar approach could be taken to bridge nano-scale irradiation damage with localisation of plasticity at microstructural length-scales in a more holistic manner.

4. Conclusions

New models describing the formation and annihilation of dislocation loops were developed and implemented in a CPFE modelling framework. The role of synergistically coupling irradiation damage, thermal variations, and mechanical loads has been investigated in the context of a Zircaloy-4 microstructure. Simulation results have shown the significance of synergistic coupling on the mechanisms involved in the initiation and localisation of plasticity, which is due to both thermal annihilation of dislocation loops, leading to softening, and the early onset of plasticity at low irradiation doses, leading to channel clearing. Thermal annihilation of dislocation loops is shown to be an important consideration, as it ultimately has a major effect on the distribution and magnitude of key damage quantities including GND density and stress. Crucially, partial coupling alone may indicate that irradiation can lead to beneficial reductions of these key quantities (compared with unirradiated material), while full coupling highlights the opposite effect.

Data availability statement

The data cannot be made publicly available upon publication because they are owned by a third party and the terms of use prevent public distribution. The data that support the findings of this study are available upon reasonable request from the authors.

Appendix. 1D sub-study of transient behaviour at various irradiation dose rates at 293 K

In this paper, a high irradiation dose rate (by industry standards [51]) is initially selected to minimise computational expense through reduced simulation time. However, this may bear implications on steady state slip resistance and strain accumulation, and ultimately, structural integrity. Hence, the results presented in this paper are contextualised in this section using a simple 1D (single slip) analysis of the evolution of dislocation loop density during irradiation and mechanical load at constant temperature; transient temperature effects are ignored here as they are not directly linked with the highly damaging channel clearing phenomenon. From equations (3)–(7), the time-dependent dislocation loop density evolution law is as follows,

$$\frac{\partial \rho_{\text{loop}}}{\partial t} = \psi^{k} \frac{\left|\dot{\gamma}^{i}\right| \sqrt{\frac{\rho_{\text{loop},t}}{N_{\langle \text{a} \rangle}}}}{b^{i}} + \frac{\eta \varphi^{-\frac{2}{3}}}{3a^{2}\bar{A}_{\text{loop}}^{2} N^{\frac{5}{3}}} \tag{A1}$$

where i corresponds to a single slip system number. The total dislocation loop density is given by numerical integration over small time increments. Using equation (1), the slip rate is calculated based on a linearly increasing resolved shear stress, τ^{i}, over a one-hour period. Similarly, three linear irradiation dose rates are selected which cover those considered in this paper as well as more industrially relevant rates (1×10^{-7} dpa s^{-1}, 1×10^{-6} dpa s^{-1}, and 1×10^{-5} dpa s^{-1}). Hardening is accounted for using equation (2) with the simplifying assumption that GND density is zero. Two stress rates, $\dot{\tau}^{i}$, and two initial dislocation loop densities are selected in this analysis, giving the following list of cases.

(a) $\dot{\tau}^{i} =$ 1/12 MPa s^{-1} from 0 to 300 MPa, with initial dislocation loop density, $\rho_{\text{loop}} = 0\ \mu\text{m}^{-2}$.
(b) $\dot{\tau}^{i} =$ 1/24 MPa s^{-1} from 150 to 300 MPa, with initial dislocation loop density, $\rho_{\text{loop}} = 0\ \mu\text{m}^{-2}$.
(c) $\dot{\tau}^{i} =$ 1/12 MPa s^{-1} from 0 to 300 MPa, with initial dislocation loop density, $\rho_{\text{loop}} = 20\ \mu\text{m}^{-2}$.
(d) $\dot{\tau}^{i} =$ 1/24 MPa s^{-1} from 150 to 300 MPa, with initial dislocation loop density, $\rho_{\text{loop}} = 20\ \mu\text{m}^{-2}$.

Figure A1 shows the evolution of dislocation loop density over time at each irradiation dose rate and for each case (a)–(d). The point at which the loop density evolution rate is zero

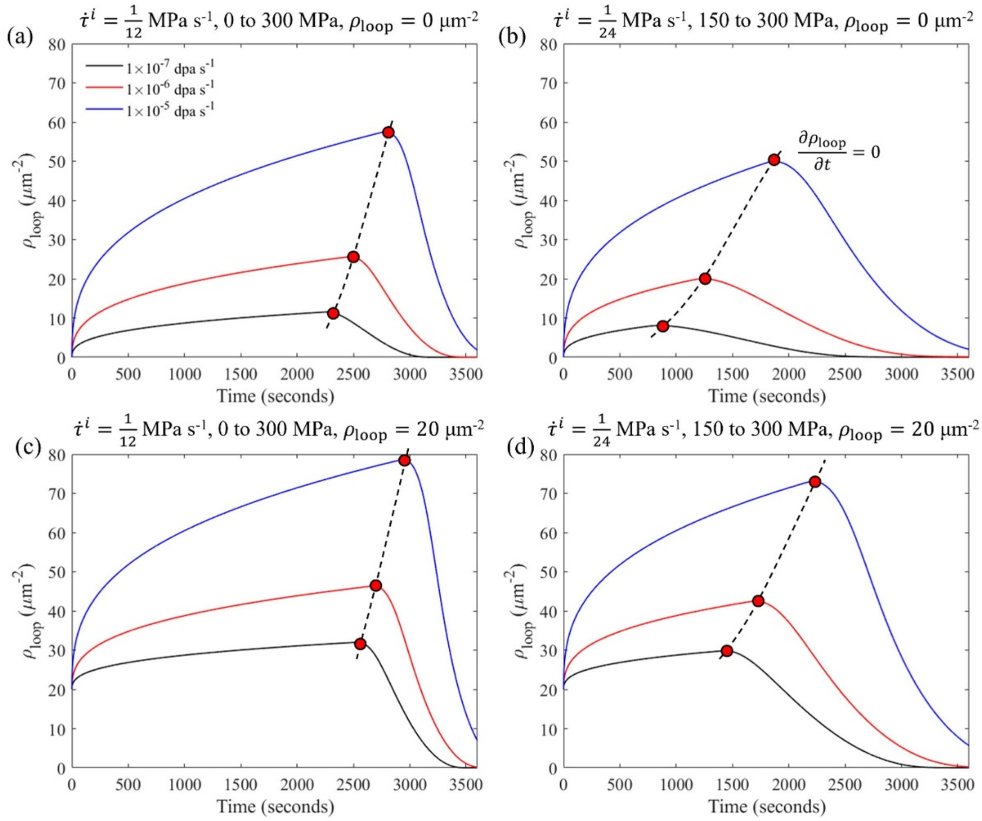

Figure A1. 1D representation of influence of irradiation damage rate on dislocation loop density evolution during synergistic mechanical load and irradiation damage at constant temperature (293 K) for cases (a)–(d).

(equilibrium point) is marked on each curve. Emphasis is placed on the equilibrium point as it is an indicator for the onset of channel clearing.

Figure A1 (a) highlights that while the irradiation damage rates selected result in significant differences in dislocation loop density evolution, the time-points at which channel clearing is likely to begin or end are less affected. Figure A1 (b) shows that the damage rate effect is heightened due to a reduced stress rate (1/24 MPa s^{-1}); although the stress range considered here is conservatively large (since the onset of plasticity leads to stress redistribution and a reduction in stress locally), this indicates that the combined selection of irradiation dose rate and stress rate can have important implications. Furthermore, figures A1 (c) and (d) highlight that hardening due to prior irradiation via an initial dislocation loop density (or e.g. GNDs), the effect of irradiation dose rate is somewhat diminished. More importantly, the resolved shear stress values at the onset of channel clearing are presented for each case in figure A2.

Despite apparently large variations in time at the onset of channel clearing, figure A2 shows that the large variations are not reflected by the resolved shear stress. The largest stress increase as a result of increased irradiation damage rate (10^{-7} dpa s^{-1}–10^{-5} dpa s^{-1}) is 20% for case (b). Hence, the implications for selecting higher dose rates are that (i) depending on the applied stress during synergistic irradiation and mechanical load, the onset of channel clearing may not be predicted where it otherwise would be within a 20% range, and contrastingly (ii) if

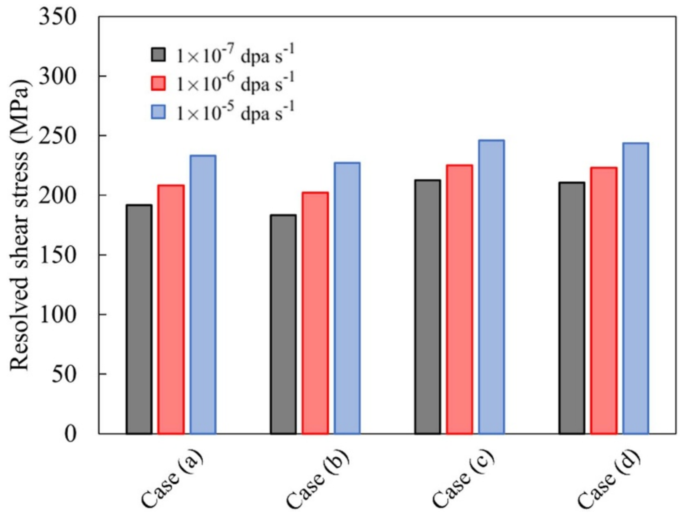

Figure A2. Resolved shear stress magnitude at transition point ($\frac{\partial \rho_{\text{loop}}}{\partial t} = 0$) for each irradiation dose rate. Cases (a)–(d) correspond to the sub-figure labels of figure A1.

stresses are sufficient to initiate channel clearing, the high stress and localised plasticity are likely to represent a worst case when considering structural integrity.

ORCID iDs

Daniel J Long https://orcid.org/0009-0004-2068-7871
Yang Liu https://orcid.org/0000-0002-9608-651X
Chris Hardie https://orcid.org/0000-0002-4852-3164

References

[1] Warwick A R *et al* 2023 Dislocation density transients and saturation in irradiated zirconium *Int. J. Plast.* **164** 103590
[2] Seymour T *et al* 2017 Evolution of dislocation structure in neutron irradiated Zircaloy-2 studied by synchrotron x-ray diffraction peak profile analysis *Acta Mater.* **126** 102–13
[3] Topping M, Ungár T, Race C P, Harte A, Garner A, Baxter F, Dumbill S, Frankel P and Preuss M 2018 Investigating the thermal stability of irradiation-induced damage in a zirconium alloy with novel in situ techniques *Acta Mater.* **145** 255–63
[4] Torimaru T, Yasuda T and Nakatsuka M 1996 Changes in mechanical properties of irradiated Zircaloy-2 fuel cladding due to short term annealing *J. Nucl. Mater.* **238** 169–74
[5] Howe L M and Thomas W R 1960 The effect of neutron irradiation on the properties of Zircaloy-2 *J. Nucl. Mater.* **2** 248–60
[6] Farrell K, Byun T S and Hashimoto N 2004 Deformation mode maps for tensile deformation of neutron-irradiated structural alloys *J. Nucl. Mater.* **335** 471–86
[7] Yasuda T, Nakatsuka M and Yamashita K 1987 Deformation and fracture properties of neutron-irradiated recrystallized Zircaloy-2 cladding under uniaxial tension *Zirconium in the Nuclear Industry* (ASTM International) pp 734–47
[8] Onimus F, Dupuy L and Mompiou F 2012 In situ TEM observation of interactions between gliding dislocations and prismatic loops in Zr-ion irradiated zirconium alloys *Prog. Nucl. Energy* **57** 77–85
[9] Weschler M S 1973 *The Inhomogeneity of Plastic Deformation* (ASM) pp 19–52

[10] Sharp J V 1967 Deformation of neutron-irradiated copper single crystals *Phil. Mag.* **16** 77–96
[11] Drouet J, Dupuy L, Onimus F and Mompiou F 2016 A direct comparison between in-situ transmission electron microscopy observations and dislocation dynamics simulations of interaction between dislocation and irradiation induced loop in a zirconium alloy *Scr. Mater.* **119** 71–75
[12] Sauzay M and Moussa M O 2013 Prediction of grain boundary stress fields and microcrack initiation induced by slip band impingement *Int. J. Fract.* **184** 215–40
[13] Moussa M O and Sauzay M 2014 Influence of thin slip bands on grain boundary stress fields and microcrack initiation: analytical and numerical approaches *Proc. Mater. Sci.* **3** 646–54
[14] Ould Moussa M and Sauzay M 2016 Introduction to the effect of the screening phenomenon of slip bands within grain microstructure *Proc. Struct. Integr.* **2** 1692–9
[15] Liu W, Chen L, Yu L, Fu J and Duan H 2022 Continuum modeling of dislocation channels in irradiated metals based on stochastic crystal plasticity *Int. J. Plast.* **151** 103211
[16] Lin P, Nie J and Liu M 2022 Multiscale crystal plasticity finite element model for investigating the irradiation hardening and defect evolution mechanism of A508-3 steel *Nucl. Mater. Energy* **32** 101214
[17] Xiao X, Li S and Yu L 2021 Effect of irradiation damage and indenter radius on pop-in and indentation stress-strain relations: crystal plasticity finite element simulation *Int. J. Mech. Sci.* **199** 106430
[18] Hardie C, Thomas R, Liu Y, Frankel P and Dunne F 2022 Simulation of crystal plasticity in irradiated metals: a case study on Zircaloy-4 *Acta Mater.* **241** 118361
[19] Thomas R *et al* 2019 Characterisation of irradiation enhanced strain localisation in a zirconium alloy *Materialia* **5** 100248
[20] Xu A, Wei T and Bhattacharyya D 2020 The effect of strain rate and orientation on He ion irradiated Ni single crystals—an in situ micro-tensile study *Int. J. Plast.* **126** 102627
[21] Packan N H, Farrell K and Stiegler J O 1978 Correlation of neutron and heavy ion damage: I. The influence of dose rate and injected helium on swelling in pure nickel *J. Nucl. Mater.* **78** 143–55
[22] Gong J, Benjamin Britton T, Cuddihy M A, Dunne F P E and Wilkinson A J 2015 (a) Prismatic, (a) basal, and (c+a) slip strengths of commercially pure Zr by micro-cantilever tests *Acta Mater.* **96** 249–57
[23] Liu Y, El Chamaa S, Wenman M R, Davies C M and Dunne F P E 2021 Hydrogen concentration and hydrides in Zircaloy-4 during cyclic thermomechanical loading *Acta Mater.* **221** 117368
[24] Xu Y 2021 A non-local methodology for geometrically necessary dislocations and application to crack tips *Int. J. Plast.* **140** 102970
[25] Ashby M F 1970 The deformation of plastically non-homogeneous materials *Phil. Mag.* **21** 399–424
[26] Xu Y, Wan W and Dunne F P E 2021 Microstructural fracture mechanics: stored energy density at fatigue cracks *J. Mech. Phys. Solids* **146** 104209
[27] Holt R A, Causey A R, Christodoulou N, Griffiths M, Ho E T C and Woo C H 1996 Non-linear irradiation growth of cold-worked Zircaloy-2 *ASTM Spec. Tech. Publ.* **1295** 623–37
[28] Dai C, Balogh L, Yao Z and Daymond M R 2016 Atomistic simulations of the formation of ⟨c⟩-type dislocation loops in α-zirconium *J. Nucl. Mater.* **478** 125–34
[29] Zheng C, Maloy S and Kaoumi D 2018 Effect of dose on irradiation-induced loop density and burgers vector in ion-irradiated ferritic/martensitic steel HT9 *Phil. Mag.* **98** 2440–56
[30] Nordlund K *et al* 2018 Improving atomic displacement and replacement calculations with physically realistic damage models *Nat. Commun.* **9** 1084
[31] Béland L K, Lu C, Osetskiy Y N, Samolyuk G D, Caro A, Wang L and Stoller R E 2016 Features of primary damage by high energy displacement cascades in concentrated Ni-based alloys *J. Appl. Phys.* **119** 085901
[32] Nordlund K *et al* 2015 *Primary Radiation Damage in Materials* (Organisation for Economic Cooperation and Developmen (OECD))
[33] Kathiria R, Wolf D E, Raj R and Jongmanns M 2021 Frenkel pairs cause elastic softening in zirconia: theory and experiments *New J. Phys.* **23** 053013
[34] Heald P T and Miller K M 1977 Point defect sink strengths in irradiated materials *J. Nucl. Mater.* **66** 107–11
[35] Derlet P M and Dudarev S L 2020 Microscopic structure of a heavily irradiated material *Phys. Rev. Mater.* **4** 023605
[36] Stoller R E and Mansur L K 1990 *The Influence of Displacement Rate on Damage Accumulation during the Point Defect Transient in Irradiated Materials* (Oak Ridge National Laboratory)

[37] Aydogan E, El-Atwani O, Li M and Maloy S A 2020 In-situ observation of nano-oxide and defect evolution in 14YWT alloys *Mater. Charact.* **170** 110686
[38] Carpenter G J C, Zee R H and Rogerson A 1988 Irradiation growth of zirconium single crystals: a review *J. Nucl. Mater.* **159** 86–100
[39] Adamson R, Griffiths M and Patterson C 2017 *Irradiation Growth of Zirconium Alloys: A Review*
[40] Eyre B L and Maher D M 1971 Neutron irradiation damage in molybdenum part V. Mechanisms of vacancy and interstitial loop growth during post-irradiation annealing *Phil. Mag.* **24** 767–97
[41] Jain A C P, Burr P A and Trinkle D R 2019 First-principles calculations of solute transport in zirconium: vacancy-mediated diffusion with metastable states and interstitial diffusion *Phys. Rev. Mater.* **3** 033402
[42] Onimus F and Béchade J L 2012 Radiation effects in zirconium alloys *Comprehensive Nuclear Materials* (Elsevier) pp 1–31
[43] Thetford R 1989 Theory of defect interactions in metals *PhD Thesis* University of Oxford, Oxford
[44] Hirth J P and Lothe J 1967 Theory of dislocations *McGraw-Hill Series in Materials Science and Engineering* (McGraw-Hill)
[45] Ribis J, Onimus F, Béchade J-L, Doriot S, Barbu A, Cappelaere C and Lemaignan C 2010 Experimental study and numerical modelling of the irradiation damage recovery in zirconium alloys *J. Nucl. Mater.* **403** 135–46
[46] Adamson R B and Bell W L 1985 Microstructure and mechanical behaviour of materials *Int. Symp. (Xian, China)* p 237
[47] Eidelpes E, Ibarra L F and Medina R A 2019 Probabilistic assessment of peak cladding hoop stress and hydrogen content of PWR SNF rod cladding *Nucl. Technol.* **205** 1095–118
[48] Zino R, Chosson R, Ollivier M, Serris E and Favergeon L 2021 Parallel mechanism of growth of the oxide and α-Zr(O) layers on Zircaloy-4 oxidized in steam at high temperatures *Corros. Sci.* **179** 109178
[49] Long F, Kerr D, Domizzi G, Wang Q and Daymond M R 2017 Microstructure characterization of a hydride blister in Zircaloy-4 by EBSD and TEM *Acta Mater.* **129** 450–61
[50] National Academies of Sciences Engineering and Medicine 2016 *Reducing the Use of Highly Enriched Uranium in Civilian Research Reactors* (The National Academies Press) (https://doi.org/10.17226/21818)
[51] Griffiths M 2021 Effect of neutron irradiation on the mechanical properties, swelling and creep of austenitic stainless steels *Materials* **14** 2622
[52] Allen T R, Cole J I, Tsai H, Ukai S, Mizuta S and Yoshitake T 1999 The effect of low dose rate irradiation on the swelling of 12% cold-worked 316 stainless steel *Newport Beach*
[53] Chen B, Jiang J and Dunne F P E 2018 Is stored energy density the primary meso-scale mechanistic driver for fatigue crack nucleation? *Int. J. Plast.* **101** 213–29
[54] Wan V V C, Maclachlan D W and Dunne F P E 2014 A stored energy criterion for fatigue crack nucleation in polycrystals *Int. J. Fatigue* **68** 90–102
[55] Yalçinkaya T, Özdemir İ and Firat A O 2019 Inter-granular cracking through strain gradient crystal plasticity and cohesive zone modeling approaches *Theor. Appl. Fract. Mech.* **103** 102306
[56] Vijay A and Sadeghi F 2022 A crystal plasticity and cohesive element model for rolling contact fatigue of bearing steels *Tribol. Int.* **173** 107607
[57] Yu Q, Chatterjee S, Roche K J, Po G and Marian J 2021 Coupling crystal plasticity and stochastic cluster dynamics models of irradiation damage in tungsten *Modelling Simul. Mater. Sci. Eng.* **29** 055021
[58] Li Y, Po G and Ghoniem N 2020 Coupled cluster-dislocation dynamics of irradiation-induced defects *Materialia* **14** 100891